Article

Probabilistic Mangrove Species Mapping with Multiple-Source Remote-Sensing Datasets Using Label Distribution Learning in Xuan Thuy National Park, Vietnam

Junshi Xia [1],*,† **, Naoto Yokoya** [1,2] **and Tien Dat Pham** [1]

1   Geoinformatics Unit, RIKEN Center for Advanced Intelligence Project (AIP), Tokyo 103-0027, Japan;
    naoto.yokoya@riken.jp (N.Y); tiendat.pham@riken.jp (T.D.P)
2   Department of Complexity of Science and Engineering, The University of Tokyo, Chiba-ken 277-8561, Japan
*   Correspondence: junshi.xia@riken.jp; Tel.: +81-3-6225-2482
†   Current address: Nihonbashi 1-Chome Mitsui Building, 15th Floor, 1-4-1 Nihonbashi, Chuo-ku,
    Tokyo 103-0027, Japan.

check for updates

Abstract: Mangrove forests play an important role in maintaining water quality, mitigating climate change impacts, and providing a wide range of ecosystem services. Effective identification of mangrove species using remote-sensing images remains a challenge. The combinations of multi-source remote-sensing datasets (with different spectral/spatial resolution) are beneficial to the improvement of mangrove tree species discrimination. In this paper, various combinations of remote-sensing datasets including Sentinel-1 dual-polarimetric synthetic aperture radar (SAR), Sentinel-2 multispectral, and Gaofen-3 full-polarimetric SAR data were used to classify the mangrove communities in Xuan Thuy National Park, Vietnam. The mixture of mangrove communities consisting of small and shrub mangrove patches is generally difficult to separate using low/medium spatial resolution. To alleviate this problem, we propose to use label distribution learning (LDL) to provide the probabilistic mapping of tree species, including *Sonneratia caseolaris* (SC), *Kandelia obovata* (KO), *Aegiceras corniculatum* (AC), *Rhizophora stylosa* (RS), and *Avicennia marina* (AM). The experimental results show that the best classification performance was achieved by an integration of Sentinel-2 and Gaofen-3 datasets, demonstrating that full-polarimetric Gaofen-3 data is superior to the dual-polarimetric Sentinel-1 data for mapping mangrove tree species in the tropics.

Keywords: mangrove species mapping; label distribution learning; Gaofen-3; Sentinel; Vietnam

1. Introduction

Mangrove ecosystems can provide a range of essential ecological services, including (1) impact reduction for natural disasters, (2) habitat provision for coastal wildlife, and (3) blue carbon sequestration in the coastal zone [1–3]. However, due to human activities and environmental degradation, mangrove forests have been significantly lost regionally and globally [4]. Thus, mapping and monitoring mangrove are imperative to building a good understanding of the current conditions, their dynamics, and further support the coastal blue carbon conservation and management [5,6].

Recently, many approaches have been proposed to map mangrove tree species using optical and synthetic aperture radar (SAR) data with various spectral/spatial/temporal resolutions [7–12]. Medium resolutions datasets, including Sentinel and Landsat series [2], have been widely used to map the changes of large areas of mangrove. With the advantages of providing more detailed spectral and texture

information, hyperspectral and high-resolution datasets are also intensively used for discriminating mangrove species. Wan et al. [13] have investigated four mangrove species in Hong Kong using the new hyperspectral Gaofen-5 dataset (330 spectral bands). Besides the conventional satellite sensors, such as Worldview [14] and Pleiades [15], unmanned aerial vehicles (UAVs) [16] have been employed for mangrove mapping, especially for individual mangrove analysis, in which the fuzzy-based and objected-based approaches are often adopted [8,12]. Since SAR images can penetrate the canopy and sensitive to the surface and vertical structure, thus, they are useful for mapping and monitoring mangrove structure and biomass [17,18]. Hence, various SAR datasets, such as ALOS, Radarsat, Sentinel-1, are used to investigate mangroves communities distribution [19–21]. Mougin et al. [22], Proisy [23] analyzed different frequencies (C-/L-/P-band) and polarizations for the mangrove tree species mapping and biomass estimation [18].

The current literature shows that multi-source remotely sensed datasets (e.g., optical, SAR and LiDAR) are able to provide complementary information [24,25], their combinations can improve the classification performance of mangrove mapping and monitoring. For instance, Souza and Paradella [26] used Radarsat SAR and Landsat optical datasets for coastal mangrove mapping in the Amazon region. Different combinations, including hyperspectral and ENVISAT SAR [27,28], multi-tidal Landsat and a Digital Elevation Model (DEM) [29], was used for mangrove tree species mapping [27,28]. Zhang et al. [1] adopted a rotation forest classifier for the mangrove tree mapping with the integration of Worldview-3 and Radarsat-2 data.

As a part of the China High-Resolution Earth Observation System (CHEOS), Gaofen-3 (GF, "High Resolution") is the first civilian C-band polarimetric SAR imaging satellite of CNSA (China National Space Administration) [30]. The GF-3 satellite has 12 imaging modes, including spotlight, stripmap, and scan, with four polarization capabilities and the highest resolution of 1 m. Previous studies have already confirmed the effectiveness of using optical Gaofen-1 [31] and Gaofen-2 [32] for the extraction of mangrove tree species. More recently, Zhu et al. [33] has integrated GF-2 Optical, GF-3 SAR, and UAV to estimate biomass of mangroves. However, the mangrove classification performance of using full-polarimetric GF-3 SAR has not yet been investigated.

In most cases, pixel-wise and objective-based classifications are employed to medium/low- and high-spatial-resolution images, respectively. However, the mixture of mangrove communities and the low spatial resolution of the datasets bring the challenge to separate mangrove tree species. In mixed-pixel studies, the sub-pixel or spectral unmixing techniques have been widely used [15,34]. However, they need the "pure" pixels (i.e., one label for one pixel) as the input. In most cases, the "pure" pixels are very hard to find in real scenarios. In such case, it is better to use soft labels (i.e., multiple labels in one pixel) instead of the one label of "pure" pixels. In this work, we propose to use a new machine learning paradigm, namely label distribution learning (LDL) [35], which uses the soft labels as the input. The label distribution covers multiple labels, representing the degree (i.e., probability) to which each label describes the pixel [35]. The objective of LDL is to predict multiple real-valued description degrees (i.e., probabilities) of the labels. The LDL methods have widely used in many machine learning applications, such as facial age estimation [36], head pose estimation [37], emotion distribution recognition [38], etc.

To date, there have been no attempts to map mangrove communities, including mixed several small and shrub mangrove patches despite these mangrove species being crucial to coastal zones in mitigating storm surges impacts and defending against rising sea levels [39]. Accordingly, the current work attempts to fill this gap by investigating multi-source optical and SAR remote sensing datasets and the label distribution learning (LDL) techniques [35] to map mangrove tree species in the mangrove ecosystem of the National Park located in North Vietnam using the combination of GF-3 SAR and optical datasets.

The main contributions are listed as follows:

1. exploiting GF-3 SAR to classify mangrove tree species for the first time.
2. investigating the combination of GF-3 full-polarimetric SAR and Sentinel-2 optical datasets.

3.   proposing to use LDL for the probabilistic mangrove species mapping.

2. Materials and Methods

2.1. Study Area

In this work, we selected the first Ramsar site in south-east Asia, namely Xuan Thuy National Park, as the study area (shown in Figure 1). It is in the Northern coastal area of Nam Dinh province, Vietnam. The study area is classified as the tropical monsoon area with two distinct dry (from November to next April) and rainy seasons (from May to October) [40].

The total area of this park is approximately 15,000 ha, of which about 7100 and 8000 ha are the core and the buffer zones, respectively. The mangrove tree densities varied at different zones of Xuan Thuy National Park, Nam Dinh Province. We observed the number of mangrove stands was higher in the core zone than those in the buffer and transition zones, ranging from 315 to 8285 tree ha $^{-1}$. The number of mangrove trees depends on the specific locations of the study area. In the buffer and transition zones, the number of trees are relatively less than in the core zone of the National Park. We counted all mangrove stands including small and shrub mangrove trees in 55 sampling plots at a size of 10 m × 10 m. We observed five dominant mangrove species, including *Sonneratia caseolaris* (SC), *Kandelia obovata* (KO), *Aegiceras corniculatum* (AC), *Rhizophora stylosa* (RS), and *Avicennia marina* (AM), during the fieldwork.
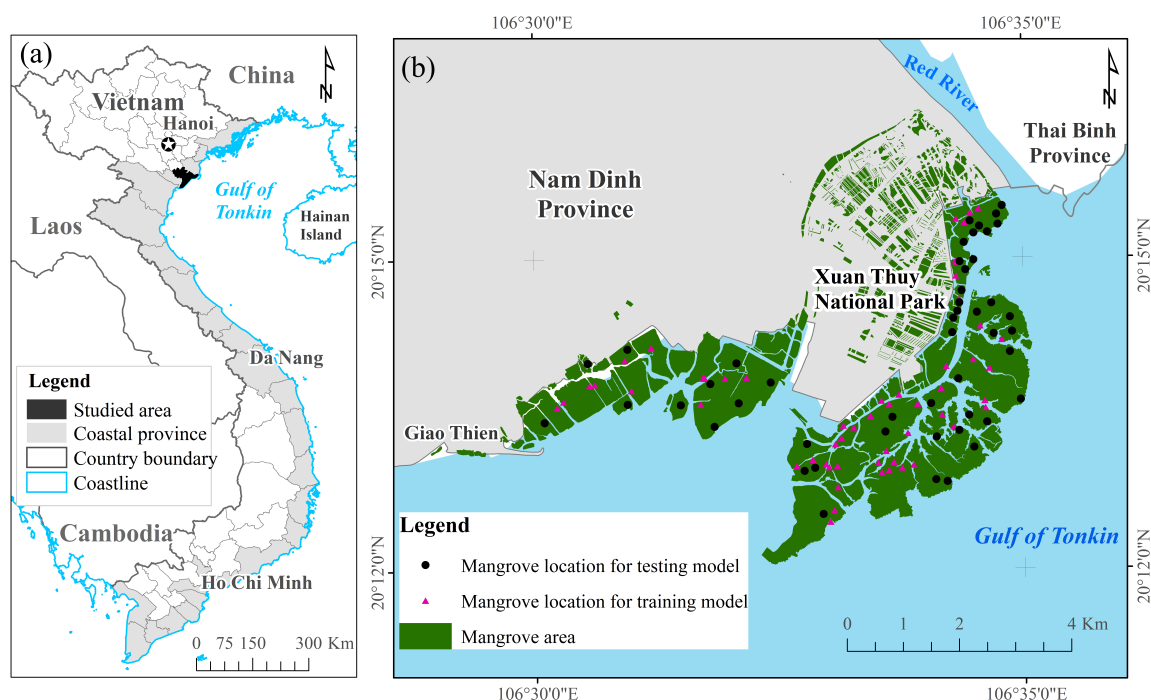

Figure 1. (**a**) The study area, Xuan Thuy National Park, is located at the estuary of the Red River in Nam Dinh province, about 150 km south east of Hanoi. (**b**) The detailed mangrove map, which was obtained from the Vietnam Forest Inventory and Planning Institute (FIPI), has shown the locations of 55 sample sites as training samples, and 71 additional sample sites as test samples.

2.2. Remote-Sensing Data

Figure 2 shows the main steps of remote-sensing image processing and the mangrove species mapping using the LDL. First, the preprocessing steps were applied to Sentinel-1, Sentinel-2 and GF-3 datasets. Furthermore, data transformation was applied to Sentinel-2 and GF-3 datasets to obtain vegetation indices and decomposition features. The probabilities derived from 55 sample sites were

used to train the LDL. Then, the probabilities map of tree species in the study area were generated. Finally, we used the descending probabilities from 71 sample sites to perform the accuracy assessment.
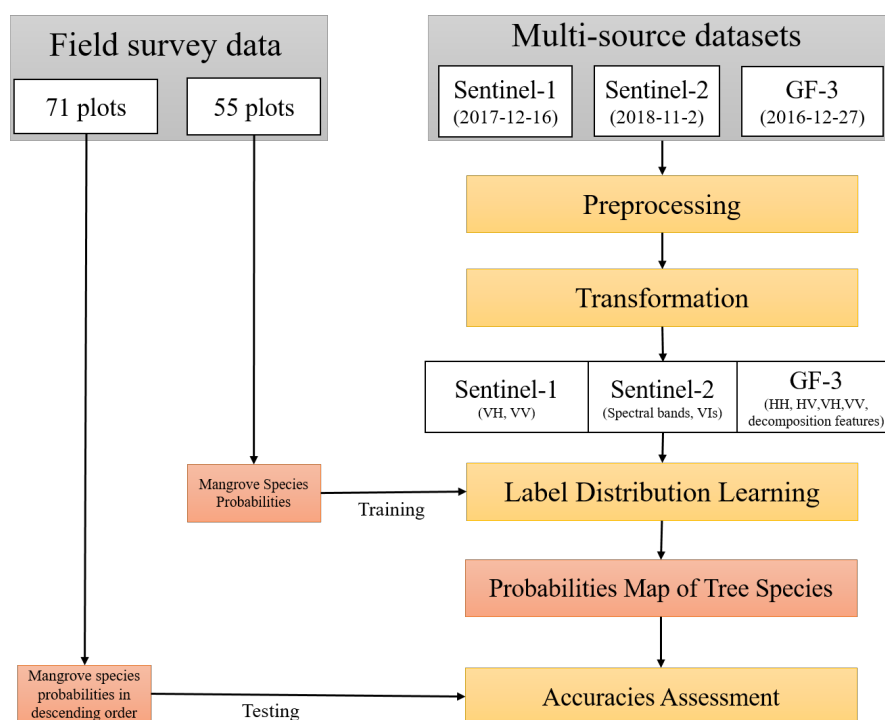

Figure 2. Flowchart of the proposed methods.

2.2.1. Remote-Sensing Pre-Processing

In this work, we selected Sentinel-1, Sentinel-2 and Gaofen-3 as the data source (Figure 3). Sentinel-1 and Sentinel-2 datasets were downloaded from the Copernicus Open Access Hub (https://scihub.copernicus.eu) run by the European Space Agency (ESA), whereas the GF-3 dataset was acquired from the China National Space Administration (CNSA).

For the Sentinel datasets, we chose the best quality images acquired in 2017 or in 2018 corresponding to the dates we did the field survey. In this case, we selected the Sentinel-2 acquired on 2 November 2018 and the Sentinel-1 dual-polarimetric SAR (VH and VV) obtained on 16 December 2017. For GF-3 datasets, we selected the full-polarimetric datasest using the acquisition mode of Quad-pol stripmap (QPSI).

GF-3 full-polarimetric SAR is very limited in this area. Since the recent GF-3 image is acquired on 27 December 2016, therefore, we selected this one in our studies. Since there is almost no change between 2016 and 2018 in this area, the influences of different dates can be ignored. The main parameters of Sentinel-1, Sentinel-2 and GF-3 are given in Table 1.

Table 1. The main parameters of the Remote-Sensing products used in this study.

Satellite	Acquisition Date	Mode	Bands	Spatial Resolution (m)
Sentinel-1	16 December 2017	Dual-Polarization	VH, VV	10
Sentinel-2	2 November 2018	Multispectral Imager (MSI)	11 spectral bands	10/20
GaoFen-3	27 December 2016	Full-Polarization	HH, HV, VH, VV	8

For the Sentinel-1 (S1) images, the following steps, including noise removal, calibration, speckle filtering, and geometric correction were applied to the VV and VH polarimetric bands and then converted to backscattering coefficients in decibel (db) unit. For the Sentinel-2 (S2) images, Sen2Cor algorithm was used for the atmospheric correction [17]. For the GF-3 datasets, the calibration constants

were used to correct the backscattering coefficient information on different polarization channels. Then, the multi-look was applied to de-speckle the image. The polarimetric coherency matrix was generated, and the refined Lee filter was used to reduce the speckle noise.
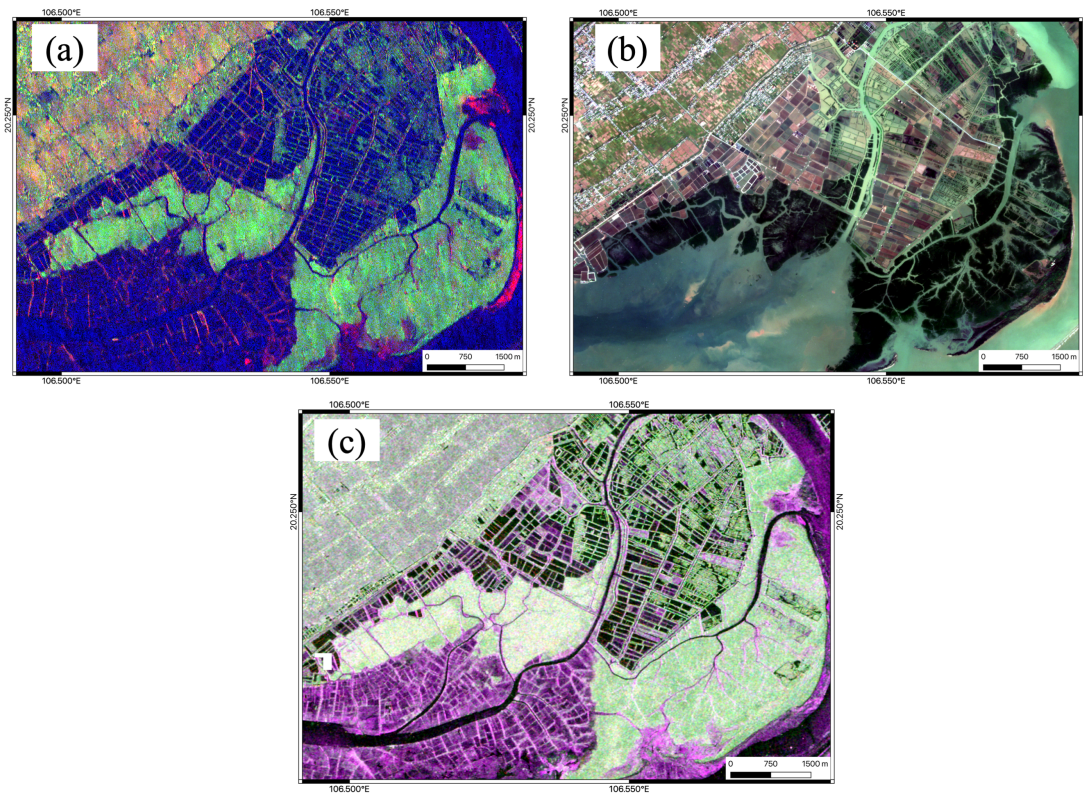

Figure 3. (**a**) False composite color image of Sentinel-1 (R:VH, G:VV, B:VV) acquired on 16 December 2017, (**b**) True composite color image of Sentinel-2 (R: Band 4, G: Band 3, B: Band 2) acquired on 2 November 2018. (**c**) False composite color image of GF-3 (R:HH, G:HV, B:VV) acquired on 27 December 2016. The land cover types surrounding the mangroves contain sea water, agriculture, tidal mudflat, salt field, built-up areas etc [41].

2.2.2. Transformation of Sentinel-2 and GF-3

In addition to spectral bands of Sentinel-2, 7 vegetation indices (VIs) derived from S2 (see in Table 2) were used in this study. It should be noted that all the spectral bands and vegetation indices (i.e., S2+VIs in short) were used as the input of the LDL methods.

Table 2. Vegetation indices used in the study.

Vegetation Index	Equation
Normalized Difference Vegetation Index (NDVI) [42]	$\frac{B8-B4}{B8+B4}$
Difference Vegetation Index (DVI) [43]	$B8-B4$
Normalized Difference Index using B4 and B5 (NDI45) [44]	$\frac{B5-B4}{B5+B4}$
Ratio Vegetation Index (RVI) [45]	$\frac{B8}{B4}$
Soil Adjusted Vegetation Index (SAVI) [46]	$1.5\frac{B8-B4}{B8+2.4B4+0.5}$
Inverted Red-Edge Chlorophyll Index (IRECI) [47]	$\frac{B7-B4}{B5/B6}$
Green Difference Vegetation Index (GNDVI) [48]	$\frac{B8-B3}{B8+B3}$

Note: B8 = NIR, B7= Vegetation red edge, B4 = Red.

For GF-3, the Pauli and Krogager decompositions [49,50] were applied to the distribution of mangrove species. Thus, in addition to four polarization channels (HH, HV, VH, VV), three Krogager components, including diplane (KD), helix (KH), and sphere (KS), three Pauli parameters, including odd-bounce scattering (P1), even-bounce scattering (P2), and volume scattering (P3), were included to map the mangrove species distribution.

Finally, we resampled all the features derived from S1, S2, and GF-3 to a resolution of 10 m to match the same size of sampling sites.

2.2.3. LDL Classification

Label Distribution Learning (LDL), which is proposed by Geng et al. [35], is a novel machine learning paradigm, aim of which is to minimize the distance between the model output and the ground-truth label distribution. In this work, we used the LDL packages from [35] (http://ldl. herokuapp.com/download).

Let us denote the degree (i.e., probability) of label y to pixel $\mathbf{x}$ by $d_{\mathbf{x}}^{y}$. The label distribution of $\mathbf{x}_i$ is given by $D_i = \{d_{\mathbf{x}_i}^{y_1}, d_{\mathbf{x}_i}^{y_2}, \dots, d_{\mathbf{x}_i}^{y_c}\}$, with the constraints of $d_{\mathbf{x}}^{y_j} \in [0,1]$ and $\sum_{j=1}^{c} d_{\mathbf{x}}^{y_j} = 1$, where c is the number of classes.

The LDL aims at predicting the probabilities of pixels or learn a conditional probability $p(y|\mathbf{x})$ from a training set $\{(\mathbf{x}_1, D_1), (\mathbf{x}_2, D_2), \dots, (\mathbf{x}_n, D_n)\}$. In general, the LDL approaches can be divided into three categories: problem transformation, algorithm adaptation, and specialized algorithms [35].

Problem transformation methods directly convert the LDL problem to the existing single-label learning (SLL) problem. In this case, problem transformation methods change the training examples into weighted single-label examples.

More specifically, each training sample $(\mathbf{x}_i, D_i)$ is transferred into c single-label samples $(\mathbf{x}_i, y_j)$ with the weights of $d_{\mathbf{x}_i}^{y_j}$. The redefined training set, which includes $c \times n$ samples, is treated as the single-label training set. In order to predict the class probability of test sample $\mathbf{x}$, the selected learning method should be able to produce the probability. In this case, two typical methods are the Bayes [51] and the support vector machines (SVMs) classifiers [52]. The former assumes the data in Gaussian distribution and uses the Bayes rule to produce the probabilities. The latter estimates the probabilities by a pairwise coupling multi-class method. Problem transformations with the Bayes and the SVMs are referred to as "PT-Bayes" and "PT-SVMs".

Algorithm adaptation extends the existing methods to deal with label distributions. In particular,the k-NN and the back-propagation neural network (BPNN) are adopted. We refer them to "AP-kNN" and "AP-BPNN", respectively. In this work, k is set to be 3.

In AP-kNN, the probability of new sample $\mathbf{x}$ is averaged by the probabilities of its k nearest neighbors:

$$p(y_j|\mathbf{x}) = \frac{1}{k} \sum_{i \in N_k(\mathbf{x})} d_{\mathbf{x}_i}^{y_j} \tag{1}$$

where $N_k(\mathbf{x})$ is the k nearest neighbors of $\mathbf{x}$.

In AP-BPNN, the SoftMax activation function was used to generate the probability output. Assume that the $j-$th output of AP-BPNN is v_j, the output z_j ($z_j \in [0,1]$ and $\sum_j z_j = 1$) is:

$$z_j = \frac{\exp(v_j)}{\sum_{k=1}^{c} \exp(v_k)}, (j = 1, 2, \dots, c) \tag{2}$$

The previous problem transformation and algorithm adaptation methods are an indirect strategy, and the performance is very limited [35,53]. In this case, we need the specialized algorithms to directly solve the LDL problem.

Suppose $p(y|\mathbf{x}; \boldsymbol{\theta})$ is a parametric model with a parameter vector $\boldsymbol{\theta}$. The two distributions can be measured by Euclidean distance, Kullback–Leibler (KL) divergence etc. If we adopt the KL divergence, the best parameter vector $\boldsymbol{\theta}^*$ can be determined in the following

$$\boldsymbol{\theta}^* = \arg\max_{\boldsymbol{\theta}} \sum_i \sum_j d_{\mathbf{x}_i}^{y_j} \ln p(y|\mathbf{x}; \boldsymbol{\theta}) \tag{3}$$

To directly tackle the optimization problem, Improved Iterative Scaling (IIS) [54] and Broyden–Fletcher–Goldfarb–Shanno (BFGS) [55] are adopted. Here, we refer to them as "SA-IIS" and "SA-BFGS", respectively. Both the methods assume $p(y|\mathbf{x}; \boldsymbol{\theta})$ to be the maximum entropy model. SA-IIS uses a strategy similar to Improved Iterative Scaling (IIS) to maximize the likelihood of the maximum entropy model. The SA-BFGS uses a quasi-Newton method BFGS as its optimization algorithm. More detailed information about the SA-IIS and the SA-BFGS techniques can be found at [35].

2.3. Field Data and Validation Analysis

Field experiments were carried out during the dry season (November and December 2018). We conducted the measurements of 55 sampling sites with a square size of 100 m^2. The geographic position was recorded using the Garmin eTreX GPS surveys. For each sampling site, all mangrove species were identified and the number of trees is counted. Also, the area of different mangrove tree species are measured.

Table 3. Probabilities of different mangrove types in 55 sample sites. The numbers of probabilities represent the area ratios. In each sample site, the sum of probabilities equals to 1.

ID	SC	KO	AC	RS	AM	ID	SC	KO	AC	RS	AM
1	0.36	0.00	0.64	0.00	0.00	29	0.00	0.33	0.67	0.00	0.00
2	0.00	0.00	1.00	0.00	0.00	30	0.00	0.80	0.20	0.00	0.00
3	0.00	0.32	0.68	0.00	0.00	31	0.00	0.96	0.04	0.00	0.00
4	0.00	0.43	0.57	0.00	0.00	32	0.00	1.00	0.00	0.00	0.00
5	0.00	0.48	0.52	0.00	0.00	33	0.00	0.52	0.48	0.00	0.00
6	0.26	0.74	0.00	0.00	0.00	34	0.00	0.76	0.24	0.00	0.00
7	0.17	0.53	0.30	0.00	0.00	35	0.00	0.65	0.35	0.00	0.00
8	0.00	0.88	0.12	0.00	0.00	36	0.00	0.83	0.17	0.00	0.00
9	0.00	0.55	0.45	0.00	0.00	37	0.00	0.40	0.60	0.00	0.00
10	0.54	0.46	0.00	0.00	0.00	38	0.36	0.00	0.64	0.00	0.00
11	0.20	0.69	0.00	0.11	0.00	39	0.23	0.00	0.77	0.00	0.00
12	0.67	0.20	0.08	0.05	0.00	40	0.00	0.48	0.52	0.00	0.00
13	0.00	1.00	0.00	0.00	0.00	41	0.00	0.90	0.10	0.00	0.00
14	0.00	0.00	0.00	1.00	0.00	42	0.38	0.00	0.62	0.00	0.00
15	0.00	0.00	0.00	0.00	1.00	43	0.35	0.00	0.65	0.00	0.00
16	0.15	0.74	0.06	0.05	0.00	44	0.00	0.67	0.00	0.33	0.00
17	0.00	1.00	0.00	0.00	0.00	45	0.00	1.00	0.00	0.00	0.00
18	0.00	0.18	0.82	0.00	0.00	46	0.00	1.00	0.00	0.00	0.00
19	0.00	0.34	0.66	0.00	0.00	47	0.00	0.82	0.00	0.18	0.00
20	0.00	0.88	0.12	0.00	0.00	48	0.00	0.61	0.00	0.39	0.00
21	0.00	0.31	0.69	0.00	0.00	49	0.00	1.00	0.00	0.00	0.00
22	0.00	1.00	0.00	0.00	0.00	50	0.00	1.00	0.00	0.00	0.00
23	0.00	0.41	0.59	0.00	0.00	51	0.00	0.90	0.00	0.10	0.00
24	0.00	0.56	0.44	0.00	0.00	52	0.00	0.99	0.00	0.01	0.00
25	0.00	0.93	0.07	0.00	0.00	53	0.00	0.96	0.00	0.04	0.00
26	0.00	0.09	0.91	0.00	0.00	54	0.00	0.95	0.00	0.05	0.00
27	0.00	0.13	0.87	0.00	0.00	55	0.00	1.00	0.00	0.00	0.00
28	0.00	1.00	0.00	0.00	0.00						

The probabilities of different mangrove types in each sample site are computed (seen in Table 3). The probabilities are the area ratios of different mangrove types. In Vietnam, there are many kinds of mangrove species; however, in the study area, five dominant species (Class 1-5) were observed during the field survey in November and December 2018, including *Sonneratia caseolaris* (SC), *Kandelia obovata* (KO), *Aegiceras corniculatum* (AC), *Rhizophora stylosa* (RS), and *Avicennia marina* (AM). As can be seen in Table 3, the mixed species of SC, KO, and AC are dominants of mangrove communities in the study area. Figure 4 depicts an example of dominant mangrove species (i.e., SC, KO, and AC), and their mixture.
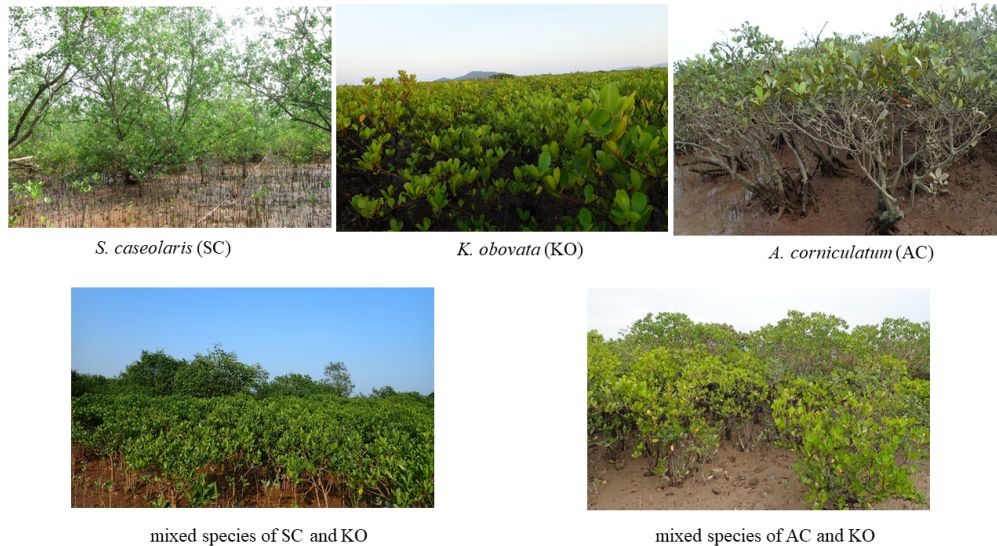

S. caseolaris (SC)　　　　*K. obovata* (KO)　　　　*A. corniculatum* (AC)

mixed species of SC and KO　　　　mixed species of AC and KO

Figure 4. The samples of dominant mangrove species (i.e., SC, KO, and AC), and their mixture in the study area. Photos were taken by T.D.P during the field survey which was conducted at Xuan Thuy National Park at latitudes 20°10′ and 20°17′N and longitude 106°25′ and 106°35′E, in November and December 2018.

We have additional 71 sample sites (a total number of 390 samples) with a size ranging from 100 m^2 to 600 m^2 generated from manual digitization and visual interpretation using very high-spatial-resolution images in Google Earth. In these sample sites, we attempted to assess the descending probabilities of tree species in each sample site. In this case, the pure types of specifies (i.e., Class 2, Class 3, Class 4 and Class 5) and the mixed types of specifies (i.e., Class 2-1, Class 2-3-1, Class 2-4, Class 3-1 and Class 3-2) are observed. Class 2-4 means the probability of Class 2 is greater than the one of Class 4. Figure 1b presents the geographic locations of these sampling sites.

Since only 55 samples with the real distribution are available, the leave-one-out cross-validation (LOOCV) technique was adopted to investigate the performance. The LOOCV uses one sample for the testing, and the remaining samples are used for the training [56]. We repeated this process 55 times to predict the accuracy of the equivalent 55 samples.

The final output of the LDL methods is the class probabilities. Followed the way introduced by [35], the following distance measures are used to evaluate the performance of leave-one-out cross validation

$$Dis_{Chebyshev}(D, \hat{D}) = \max_j | d_j - \hat{d}_j | \tag{4}$$

$$Dis_{Clark}(D, \hat{D}) = \sqrt{\sum_{j=1}^{c} \frac{(d_j - \hat{d}_j)^2}{(d_j + \hat{d}_j)^2}} \tag{5}$$

$$Dis_{Canberra}(D, \hat{D}) = \sqrt{\sum_{j=1}^{c} \frac{|d_j - \hat{d}_j|}{d_j + \hat{d}_j}} \tag{6}$$

$$Dis_{KL}(D, \hat{D}) = \sum_{j=1}^{c} d_j \ln \frac{d_j}{\hat{d}_j} \tag{7}$$

$$Dis_{Cos}(D, \hat{D}) = \frac{\sum_{j=1}^{c} d_j \hat{d}_j}{\sqrt{\sum_{j=1}^{c} d_j^2} \sqrt{\sum_{j=1}^{c} \hat{d}_j^2}} \tag{8}$$

$$Dis_{Intersection}(D, \hat{D}) = \min(d_j, \hat{d}_j) \tag{9}$$

The additional 71 sample sites consisted of a total number of 390 samples with the descending probabilities were used to evaluate the pixel-wise accuracy. For the individual class, the pixel is correctly classified when the probability is higher than 0.7. For the mixture, the pixel is correctly classified when the descending order of each tree species' probabilities are the same as the validation ones.

To investigate the influence of the input features on mangrove mapping accuracy, we conducted the five experiments as the following. In the first experiment, the variables derived from the S2 multispectral bands and VIs were included. In the second experiment, the 22 variables through a combination of S2 and S1 (S1+S2+VIs) were used. In the third experiment, the 24 variables derived from S2 and GF-3 four backscattering coefficients (S2+VIs+GF-3 (4)) were used. In the fourth experiment, the 30 variables through a combination of S2 and GF-3 all variables (S2+VIs+GF-3 (all)) were used. In the fifth experiment, all the variables derived from S1, S2, and GF-3 (S1+S2+VIs+GF-3 (all)) were included.

3. Results

3.1. Results with Different LDL Methods

We evaluated the performance of six different LDL methods using the combination of spectral bands and VIs derived from Sentinel-2 as the input features (Table 4). The SA-BFGS provides the best classification results, followed by SA-IIS > PT-Bayes > AA-KNN > AA-BP > PT-SVMs.

The PT-Bayes yields good results on the measures 'Chebyshev' and 'Intersection'. The SA-IIS technique has good results on the measures of 'Clark', 'Canberra', and 'Cos'. The SA-IIS and the SA-BFGS methods share the top positions because they directly minimize the distance between the probabilities of training and test samples. The main reasons for the lower accuracies of the PT-SVMs and the AA-BPNN are two folds: (1) very limited training samples, and (2) over-fitting with more tuned parameters.

Table 4. Measures on the distance metric.

Measure	PT-Bayes	PT-SVMs	AA-KNN	AA-BPNN	SA-IIS	SA-BFGS
Chebyshev ($\downarrow$)	0.3495	0.5339	0.3890	0.4372	0.3950	0.2346
Clark ($\downarrow$)	2.0113	1.9479	1.8978	1.9043	1.8810	1.8736
Canberra ($\downarrow$)	4.2004	4.0894	4.1231	3.9366	3.8553	3.7498
KL ($\downarrow$)	0.065	0.084	0.078	0.082	0.045	0.034
Cos ($\uparrow$)	0.7466	0.5555	0.7472	0.7238	0.7721	0.8778
Intersection ($\uparrow$)	0.6407	0.4374	0.5999	0.5466	0.5904	0.7548

Table 5 reveals the results of different ascending order combination of tree species on the additional validation of 71 sample sites. It should be noted that Class 2, 3, 4, 5 are the pure classes, and Class 2-1, Class 2-3-1, Class 2-4, Class 3-1 and Class 3-2 are the mixed classes. Class 2-1 means that the probability of Class 2 is greater than the one of Class 1. From this Table, it can be clearly seen that the PT-Bayes,

the PT-SVMs, the AA-KNN, the AA-BP, the SA-IIS algorithms cannot predict the pure Class 3, 4, 5. PT-Bayes can give the best result of Class 2. The AA-BP and the SA-IIS yield excellent performance on the mixed classes (2-3, 2-3-1, 2-4, 3-1). The SA-BFGS can balance the accuracies between pure and mixed classes. Considering the accuracies of pure and mixed classes, the ranking of the algorithms is SA-BFGS > AA-BPNN > SA-IIS > AA-KNN > PT-SVMs = PT-Bayes. The SA-BFGS performs better than other methods because it improves the performance of the SA-IIS by using more effective optimization process. Therefore, the SA-BFGS is selected to analyze the combination of different source images.

Table 5. Accuracy assessment on the additional 71 plots with different LDL methods.

Class	No. Samples	PT-Bayes	PT-SVMs	AA-KNN	AA-BPNN	SA-IIS	SA-BFGS
2	63	98.41	0	20.63	6.35	6.35	47.62
3	32	3.13	0	0	0	0	6.25
4	10	0	0	0	0	0	60.00
5	4	0	0	0	0	0	25.00
2-1	25	0	0	60.00	96.00	100.00	92.00
2-3-1	4	25.00	100.00	100.00	75.00	75.00	25.00
2-4	63	0	96.83	47.62	79.31	87.30	36.51
3-1	79	0	0	64.56	79.71	65.81	64.56
3-2	110	5.45	0	15.45	24.55	0	34.55
Overall accuracy (OA)		17.95	16.67	33.33	43.83	35.64	44.87
Average accuracy (AA)		15.81	21.87	34.25	40.10	37.16	43.50

3.2. Results with Different Sources of Datasets

Five classification were produced using (1) S2 spectral bands and VIs (S2+VIs), (2) a combination of S2 optical, VIs and S1 (S1+S2+VIs), (3) a combination of S2 and GF-3 four backscattering coefficients (S2+VIs+GF-3 (4)), (4) a combination of S2 and GF-3 all variables (S2+VIs+GF-3 (all)), (5) a combination of S1, S2, and GF-3 (S1+S2+VIs+GF-3 (all)).

We performed an accuracy assessment using the additional 71 sample sites with the overall accuracies (OAs) of 44.82% (S2+VIs), 46.66%(S2+VIs+S1), 59.49%(S2+VIs+GF-3 (4)), 58.50% (S2+VIs+GF3 (all)), 53.36 % (S1+S2+VIs+GF3 (all)) and with the AAs of 43.49% (S2+VIs), 46.31%(S2+VIs+S1), 51.90%(S2+VIs+GF3 (4)), 49.19% (S2+VIs+GF3 (all)), 45.94% (S1+S2+VIs+GF3 (all)). Among all the combinations, S2+VIs+GF3 (4) obtained the best results, and the probabilities maps are shown in Figure 5. This observation demonstrated that the full-polarimetric GF-3 SAR could provide more beneficial information than dual-polarimetric S1 SAR when combining with S2 optical data to improve the classification accuracy of probabilistic mangrove species mapping.

To further in-depth analyze the complementary information from SAR datasets regarding pure or mixed types of mangrove tree species, we list the individual accuracy in Table 6. This table indicates that pure Class 4, mixed Class 2-1, and 3-1 (with accuracy > 60%) are easily identified compared to other tree species. All the combinations can obtain adequate accuracies. The performance of pure Class 5, and the mixed Class 2-3-1, Class 3-2 were much lower due to the limited training samples. With the addition of dual-polarimetric Sentinel-1, the accuracies of Class 3 and Class 2-4 were noticeably increased. However, the accuracies of Class 2, 2-1, 3-1, 3-2 decreased. Furthermore, combining the full-polarimetric GF-3, all the classes, except Class 4, 5, 2-3-1, improved the performance significantly. For instance, the accuracies of Class 2 and Class 2-4 increased to 56.25% and 96.83% from 6.25% and 36.28%, respectively. With the help of Pauli and Krogager decomposition, the accuracies of pure Class 2 and Class 3 increased, but the performance of mixed Class 2-4, 3-1, and 3-2 decreased.
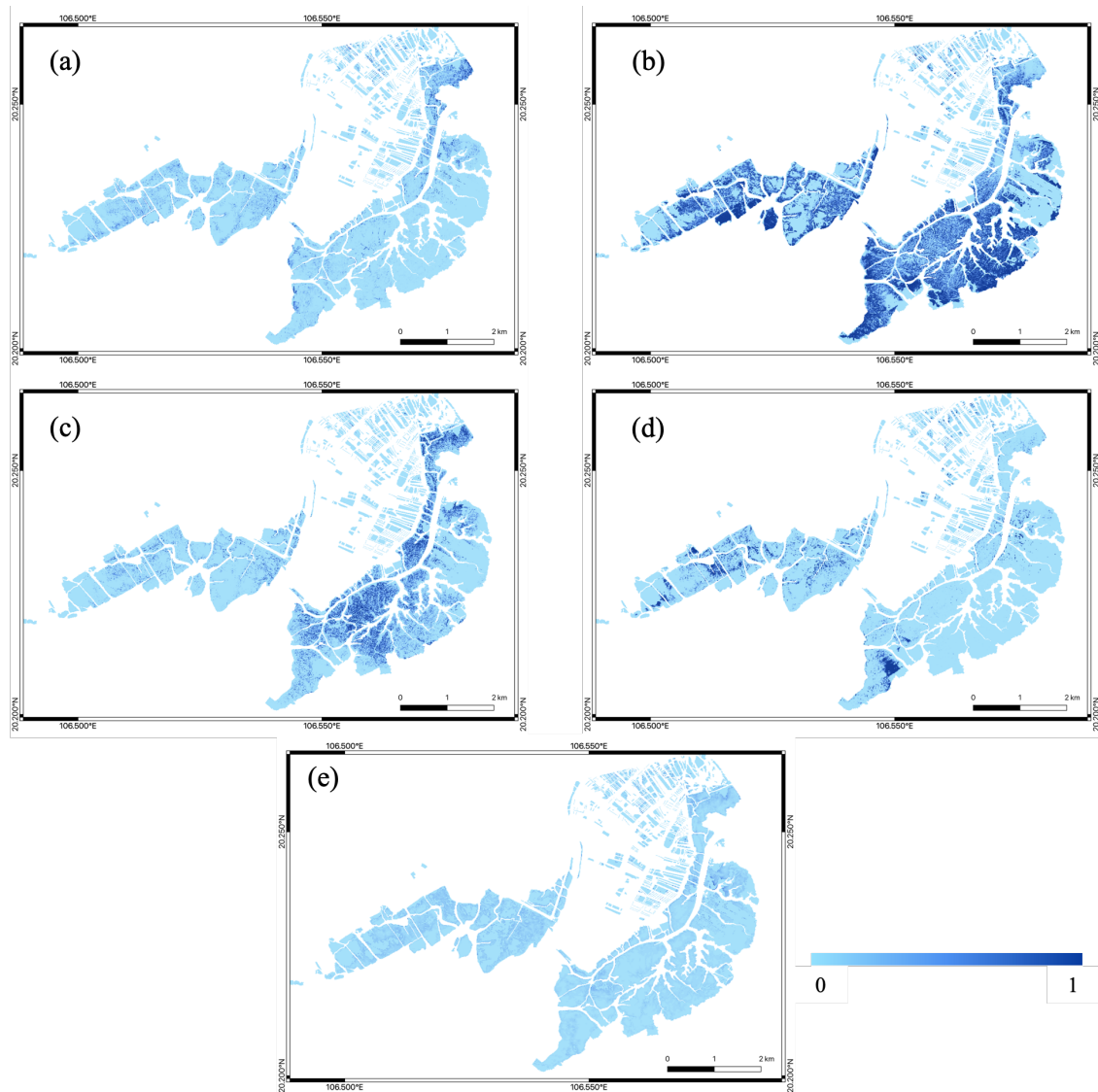
Figure 5. Probability maps of (**a**) *Sonneratia caseolaris* (SC), (**b**) *Kandelia obovata* (KO), (**c**) *Aegiceras corniculatum* (AC), (**d**) *Rhizophora stylosa* (RS), (**e**) *Avicennia marina* (AM) generated by the best performance (OA: 62.44%, AA: 51.90%) using the specialized algorithm with BFGS optimization (SA-BFGS) and the combination of spectral bands, vegetation indices of Sentinel-2, and four polarization channels of Gaofen-3, which is short for S2+VIs+GF(4) in the manuscript.

Table 6. Accuracy assessment on the additional 71 plots with different combinations of multiple-source datasets.

Class	No. Samples	S2+VIs	S1+S2+VIs	S2+VIs+GF (4)	S2+VIs+GF (All)	S1+S2+VIs+GF (All)
2	63	47.62	44.44	50.79	53.97	47.61
3	32	6.25	53.13	56.25	62.50	50.00
4	10	60.00	60.00	60.00	60.00	60.00
5	4	25.00	25.00	25.00	25.00	25.00
2-1	25	92.00	72.00	80.00	64.00	64.00
2-3-1	4	25.00	25.00	25.00	25.00	25.00
2-4	63	36.51	42.85	63.49	52.38	49.20
3-1	79	64.56	60.76	68.35	63.29	60.76
3-2	110	34.55	33.64	38.18	36.36	31.82
Overall accuracy (OA)		44.87	46.66	62.44	58.50	53.36
Average accuracy (AA)		43.49	46.31	51.90	49.19	45.94

4. Discussion

4.1. Contribution from the Full-Polarimetric SAR

Mangrove mapping with the combination of optical and SAR datasets has been reported by previous studies [1,21,27] and few studies have investigated the classification performance with full-pol SAR (e.g., RADARSAT-2 and ALOS-PALSAR-2) [57,58].

In this work, the complementary role of full-polarimetric GF-3 SAR towards optical data was tested and assessed for the improvement of mangrove tree species probabilistic mapping. As we expected, the OAs were improved from 44.87% (S2+VIs) to 46.66% (S2+VIs+S1) and 62.44% (S2+VIs+GF-3 (4)), while the AAs was improved from 43.49%(S2+VIs) to 46.31% (S2+VIs+S1) and 52.90% (S2+VIs+GF-3 (4)). This improvement can be further explained from the individual accuracies over different kinds of tree species, showing that GF-3 full-pol SAR may improve the identification capability of not only the pure types but also the mixed combinations when compared to the dual-pol SAR. Pauli and Krogager decomposition were included; the classification accuracies of the pure types of mangrove tree specifies are improved. In future studies, we will compare the performance of L-band and C-band full-pol SAR and investigate the potential joint use of multifrequency full-pol SAR.

4.2. Factors Affecting Accuracy Assessment

In a real case, very limited reference samples are typical. Collecting many samples under mangrove ecosystems is extremely difficult, time-consuming, and costly. In this study, only 55 samples with the probabilities collected by the field survey were used for the training, and the additional 71 sample sites (390 samples) were used for the validation. From a statistical point of view, this very limited training sample size may decrease reliability. In this work, the classification performance derived from the combined full-pol GF-3 SAR and optical (S2+VIs) using SA-BFGS are significantly better than others from only optical and the combined dual-pol SAR and optical with all applied method.

In machine learning community, active learning and semi-supervised learning are often adopted to deal with limited training samples. There have been a few attempts to use semi-supervised learning technique for the mangrove mapping. For instance, Silva et al. [59] proposed to use cost-sensitive and semi-supervised learning to classify mangrove in Saloum estuary, Senegal, from Landsat imagery. Weinstein et al. [60] developed semi-supervised deep learning neural networks to detect individual tree from Airborne RGB images. In the future, we may consider including active learning and semi-supervised learning to further improve the performance.

4.3. Investigations about Combinations and Methods

The accurate assessment for the spatial distribution of mangrove communities, which consisted of mixed species, particularly small and shrubs patches, is still a challenging task. In this work, we investigate and compare the different combination of full-pol SAR, dual-pol SAR and optical data for probabilistic mangrove mapping.

Two advantages need to be considered. First, regarding the SAR datasets, more and more free public SAR datasets (e.g., Sentinel-1) are used to increasing the accuracy of mangrove mapping, full-pol GF-3 datasets are used in this work. Experimental results indicated better performance using full-pol SAR rather than dual-pol SAR because full-pol SAR could provide more informative features to classify the different dominant or mixed tree species.

Second, regarding the methodology, most studies worked on mangrove species mapping using medium resolution images is a pixel-wise method. Due to limited spatial resolution, the mixed tree species in one pixel often exist. Traditionally the most used approach to deal with the mixed pixel is the sub-pixel analysis or spectral unmixing [15,34]. In all existing spectral unmixing or sub-pixel methods, the "pure" pixel should be found. Contrary to these methods, we employed the LDL methods, which do not need the "pure" pixel and use the probabilistic as the input. We expected that

it could be more useful than the pixel-wise classifier to generate the probabilistic classification maps. More specifically, three typical kinds of methods were compared: problem transformations (PT-Bayes and PT-SVM), algorithm adaptation (AA-kNN and AA-BPNN), and specialized algorithm (SA-IIS and SA-BFGS). As observed from the experiments, the SA methods are better than those of other methods by considering the accuracy of individual and mixed tree species. When including the full-pol SAR datasets, the accuracy is further improved.

4.4. Limitation of This Study

Mangroves distribution mapping can be divided into two parts: extent mapping (mangroves or non-mangroves) and species distribution mapping [5]. Extent mapping can be done by coarse or medium resolution remote-sensing datasets, such as Landsat and Sentinel, while mangrove tree species mapping should be obtained from high-spatial-resolution datasets, including IKONOS. Now, all the studies of mangrove tree species mapping are conducted in a local scale, the species distribution at continental or global scale is missing.

In this work, we attempt to use LDL methods to produce probability mapping of mangrove tree species with multi-source datasets. The results encourage us to further extend LDL to large-scale mapping. However, the main limitation of this study is the very limited training samples with probabilities. LDL methods require very accurate training samples.

5. Conclusions

This is the first study attempted to investigate the potential of the combined optical and full-polarimetric SAR remote-sensing data for mapping probabilities of mangrove communities including mixed several small mangrove species using the LDL approaches in Xuan Thuy National park located in North Vietnam. Various combinations of remote-sensing datasets, including Sentinel-1 dual-polarimetric SAR, Sentinel-2 multispectral, and Gaofen-3 full-polarimetric SAR, were investigated. Then, different types LDL methods were applied to classify the mangrove tree species. Experimental results demonstrated that a combination of spectral bands and all vegetation indices (e.g., NDVI, DVI, NDI45, RVI, SAVI, IRECI and GNDVI) derived from Sentinel-2 and four polarization channels of Gaofen-3, which is short for S2+VIs+GF(4), obtained the best performance.

Dual-polarimetric Sentinel-1 SAR data was beneficial to improve the classification of *Aegiceras corniculatum* (AC) species. However, the accuracies of the most mixed combination of tree species, such as the mixture of *Sonneratia caseolaris* (SC) and *Kandelia obovata* (KO) species, decreased. Finally, full-polarimetric SAR datasets tend to improve the accuracy of both pure and mixed types of tree species. For the method, the best accuracies were obtained by the specialized algorithms (SA) with Broyden–Fletcher–Goldfarb–Shanno (BFGS) optimization (SA-BFGS). The methods used in this study can apply for mapping mangrove communities on a large scale due to the efficient computation time (less than one minute on a computer with Intel Core i7 CPU, 1.30 GHz, and 32 GB of memory). The main reason for such efficiency is that the method adopts the efficient BFGS optimization method, whose computation is related to the to the first-order gradient, performing much more efficiently than the standard line search Newton method (e.g., IIS) based on previous studies [35,61,62]. These findings indicate the reliability of the LDL method for mapping the probabilistic mangrove species distribution and may provide a road-map using multi-source datasets and the LDL algorithms in other remote-sensing applications.

Conflicts of Interest: The authors declare no conflict of interest.

References

1. Zhang, H.; Wang, T.; Liu, M.; Jia, M.; Lin, H.; Chu, L.M.; Devlin, A.T. Potential of Combining Optical and Dual Polarimetric SAR Data for Improving Mangrove Species Discrimination Using Rotation Forest. *Remote Sens.* **2018**, *10*, 467. [CrossRef]

2. Wang, D.; Wan, B.; Qiu, P.; Su, Y.; Guo, Q.; Wang, R.; Sun, F.; Wu, X. Evaluating the Performance of Sentinel-2, Landsat 8 and Pléiades-1 in Mapping Mangrove Extent and Species. *Remote Sens.* **2018**, *10*, 1468. [CrossRef]

3. Künzer, C.; Bluemel, A.; Gebhardt, S.; Quoc, T.V.; Dech, S. Remote Sensing of Mangrove Ecosystems: A Review. *Remote Sens.* **2011**, *3*, 878–928. [CrossRef]

4. Ahmed, N.; Glaser, M. Coastal aquaculture, mangrove deforestation and blue carbon emissions: Is REDD+ a solution? *Mar. Policy* **2016**, *66*, 58–66. [CrossRef]

5. Wang, L.; Jia, M.; Yin, D.; Tian, J. A review of remote sensing for mangrove forests: 1956–2018. *Remote Sens. Environ.* **2019**, *231*, 111223. [CrossRef]

6. Pham, T.D.; Xia, J.; Ha, N.T.; Bui, D.T.; Le, N.N.; Takeuchi, W. A Review of Remote Sensing Approaches for Monitoring Blue Carbon Ecosystems: Mangroves, Seagrasses and Salt Marshes during 2010–2018. *Sensors* **2019**, *19*, 1933. [CrossRef] [PubMed]

7. Wan, L.; Zhang, H.; Liu, M.; Lin, Y.; Lin, H. Early Monitoring of Exotic Mangrove Sonneratia in Hong Kong Using Deep Convolutional Network at Half-Meter Resolution. *IEEE Geosci. Remote Sens. Lett.* **2020**, in press. [CrossRef]

8. He, Z.; Shi, Q.; Liu, K.; Cao, J.; Zhan, W.; Cao, B. Object-Oriented Mangrove Species Classification Using Hyperspectral Data and 3-D Siamese Residual Network. *IEEE Geosci. Remote Sens. Lett.* **2020**, in press. [CrossRef]

9. Chakravortty, S.; Li, J.; Plaza, A. A Technique for Subpixel Analysis of Dynamic Mangrove Ecosystems With Time-Series Hyperspectral Image Data. *IEEE J. Sel. Top. Appl. Earth Obs. Remote Sens.* **2018**, *11*, 1244–1252. [CrossRef]

10. Jia, M.; Wang, Z.; Zhang, Y.; Ren, C.; Song, K. Landsat-Based Estimation of Mangrove Forest Loss and Restoration in Guangxi Province, China, Influenced by Human and Natural Factors. *IEEE J. Sel. Top. Appl. Earth Obs. Remote Sens.* **2015**, *8*, 311–323. [CrossRef]

11. Viennois, G.; Proisy, C.; Féret, J.; Prosperi, J.; Sidik, F.; Suhardjono; Rahmania, R.; Longépé, N.; Germain, O.; Gaspar, P. Multitemporal Analysis of High-Spatial-Resolution Optical Satellite Imagery for Mangrove Species Mapping in Bali, Indonesia. *IEEE J. Sel. Top. Appl. Earth Obs. Remote Sens.* **2016**, *9*, 3680–3686. [CrossRef]

12. Son, N.; Chen, C.; Chang, N.; Chen, C.; Chang, L.; Thanh, B. Mangrove Mapping and Change Detection in Ca Mau Peninsula, Vietnam, Using Landsat Data and Object-Based Image Analysis. *IEEE J. Sel. Top. Appl. Earth Obs. Remote Sens.* **2015**, *8*, 503–510. [CrossRef]

13. Wan, L.; Lin, Y.; Zhang, H.; Wang, F.; Liu, M.; Lin, H. GF-5 Hyperspectral Data for Species Mapping of Mangrove in Mai Po, Hong Kong. *Remote Sens.* **2020**, *12*, 656. [CrossRef]

14. McCarthy, M.J.; Jessen, B.; Barry, M.J.; Figueroa, M.; McIntosh, J.; Murray, T.; Schmid, J.; Muller-Karger, F.E. Automated High-Resolution Time Series Mapping of Mangrove Forests Damaged by Hurricane Irma in Southwest Florida. *Remote Sens.* **2020**, *12*, 1740. [CrossRef]

15. Taureau, F.; Robin, M.; Proisy, C.; Fromard, F.; Imbert, D.; Debaine, F. Mapping the Mangrove Forest Canopy Using Spectral Unmixing of Very High Spatial Resolution Satellite Images. *Remote Sens.* **2019**, *11*, 367. [CrossRef]

16. Individual mangrove tree measurement using UAV-based LiDAR data: Possibilities and challenges. *Remote Sens. Environ.* **2019**, *223*, 34–49. [CrossRef]

17. Pham, T.D.; Yokoya, N.; Xia, J.; Ha, N.T.; Le, N.N.; Nguyen, T.T.T.; Dao, T.H.; Vu, T.T.P.; Pham, T.D.; Takeuchi, W. Comparison of Machine Learning Methods for Estimating Mangrove Above-Ground Biomass Using Multiple Source Remote Sensing Data in the Red River Delta Biosphere Reserve, Vietnam. *Remote Sens.* **2020**, *12*, 1334. [CrossRef]

18. Pham, T.D.; Yokoya, N.; Bui, D.T.; Yoshino, K.; Friess, D.A. Remote Sensing Approaches for Monitoring Mangrove Species, Structure, and Biomass: Opportunities and Challenges. *Remote Sens.* **2019**, *11*, 230. [CrossRef]

19. Hamdan, O.; Khali Aziz, H.; Mohd Hasmadi, I. L-band ALOS PALSAR for biomass estimation of Matang Mangroves, Malaysia. *Remote Sens. Environ.* **2014**, *155*, 69–78. [CrossRef]

20. Kovacs, J.M.; Vandenberg, C.V.; Wang, J.; Flores-Verdugo, F. The Use of Multipolarized Spaceborne SAR Backscatter for Monitoring the Health of a Degraded Mangrove Forest. *J. Coast. Res.* **2008**, *241*, 248–254. [CrossRef]

21. Pham, T.D.; Yoshino, K.; Kaida, N. Monitoring Mangrove Forest Changes in Cat Ba Biosphere Reserve Using ALOS PALSAR Imagery and a GIS-Based Support Vector Machine Algorithm. In *Advances and Applications in Geospatial Technology and Earth Resources*; Tien Bui, D., Ngoc Do, A., Bui, H.B., Hoang, N.D., Eds.; Springer International Publishing: Cham, Switzerland, 2018; pp. 103–118.

22. Mougin, E.; Proisy, C.; Marty, G.; Fromard, F.; Puig, H.; Betoulle, J.L.; Rudant, J.P. Multifrequency and multipolarization radar backscattering from mangrove forests. *IEEE Trans. Geosci. Remote Sens.* **1999**, *37*, 94–102. [CrossRef]

23. Proisy, C. Interpretation of Polarimetric Radar Signatures of Mangrove Forests. *Remote Sens. Environ.* **2000**, *71*, 56–66. [CrossRef]

24. Zhang, H.; Xu, R. Exploring the optimal integration levels between SAR and optical data for better urban land cover mapping in the Pearl River Delta. *Int. J. Appl. Earth Obs. Geoinf.* **2018**, *64*, 87–95. [CrossRef]

25. Zhang, H.; Lin, H.; Li, Y.; Zhang, Y.; Fang, C. Mapping urban impervious surface with dual-polarimetric SAR data: An improved method. *Landsc. Urban Plan.* **2016**, *151*, 55–63. [CrossRef]

26. Souza, P.; Paradella, W. Use of Radarsat-1 fine mode and Landsat-5 TM selective principal component analysis for geomorphological mapping in a macrotidal mangrove coast in the amazon region. *Can. J. Remote Sens.* **2005**, *31*, 214–224. [CrossRef]

27. Wong, F.K.K.; Fung, T. Combining Hyperspectral and Radar Imagery for Mangrove Leaf Area Index Modeling. *Photogramm. Eng. Remote Sens.* **2013**, *79*, 479–490. [CrossRef]

28. Wong, F.K.K.; Fung, T. Combining EO-1 Hyperion and Envisat ASAR data for mangrove species classification in Mai Po Ramsar Site, Hong Kong. *Int. J. Remote Sens.* **2014**, *35*, 7828–7856. [CrossRef]

29. Zhang, X.; Treitz, P.M.; Chen, D.; Quan, C.; Shi, L.; Li, X. Mapping mangrove forests using multi-tidal remotely-sensed data and a decision-tree-based procedure. *Int. J. Appl. Earth Obs. Geoinf.* **2017**, *62*, 201–214. [CrossRef]

30. Xu, L.; Zhang, H.; Wang, C.; Fu, Q. Classification of Chinese GaoFen-3 fully-polarimetric SAR images: Initial results. In Proceedings of the 2017 Progress in Electromagnetics Research Symposium—Fall (PIERS-FALL), Singapore, 19–22 November 2017; pp. 700–705.

31. Liu, M.; Li, H.; Li, L.; Man, W.; Jia, M.; Wang, Z.; Lu, C. Monitoring the Invasion of Spartina alterniflora Using Multi-source High-resolution Imagery in the Zhangjiang Estuary, China. *Remote Sens.* **2017**, *9*, 539. [CrossRef]

32. Peng, L.; Liu, K.; Cao, J.; Zhu, Y.; Li, F.; Liu, L. Combining GF-2 and RapidEye satellite data for mapping mangrove species using ensemble machine-learning methods. *Int. J. Remote Sens.* **2020**, *41*, 813–838. [CrossRef]

33. Zhu, Y.; Liu, K.W.; Myint, S.; Du, Z.; Li, Y.; Cao, J.; Liu, L.; Wu, Z. Integration of GF2 Optical, GF3 SAR, and UAV Data for Estimating Aboveground Biomass of China's Largest Artificially Planted Mangroves. *Remote Sens.* **2020**, *12*, 2039. [CrossRef]

34. Kamal, M.; Phinn, S. Hyperspectral Data for Mangrove Species Mapping: A Comparison of Pixel-Based and Object-Based Approach. *Remote Sens.* **2011**, *3*, 2222–2242. [CrossRef]

35. Geng, X. Label Distribution Learning. *IEEE Trans. Knowl. Data Eng.* **2016**, *28*, 1734–1748. [CrossRef]

36. Geng, X.; Yin, C.; Zhou, Z.H. Facial Age Estimation by Learning from Label Distributions. *IEEE Trans. Pattern Anal. Mach. Intell.* **2013**, *35*, 2401–2412. [CrossRef] [PubMed]

37. Geng, X.; Xia, Y. *Head Pose Estimation Based on Multivariate Label Distribution*; CVPR; IEEE Computer Society: Columbus, OH, USA, 2014; pp. 1837–1842.

38. Zhou, Y.; Xue, H.; Geng, X. Emotion Distribution Recognition from Facial Expressions. In *ACM Multimedia*; Zhou, X., Smeaton, A.F., Tian, Q., Bulterman, D.C.A., Shen, H.T., Mayer-Patel, K., Yan, S., Eds.; ACM: Brisbane, Australia, 2015; pp. 1247–1250.

39. Curnick, D.J.; Pettorelli, N.; Amir, A.A.; Balke, T.; Barbier, E.B.; Crooks, S.; Dahdouh-Guebas, F.; Duncan, C.; Endsor, C.; Friess, D.A.; et al. The value of small mangrove patches. *Science* **2019**, *363*, 239. [PubMed]

40. Veettil, B.K.; Ward, R.D.; Quang, N.X.; Trang, N.T.T.; Giang, T.H. Mangroves of Vietnam: Historical development, current state of research and future threats. *Estuar. Coast. Shelf Sci.* **2019**, *218*, 212–236. [CrossRef]

41. Nguyen, T.T.N.; Tran, H.C.; Ho, T.M.H.; Burny, P.; Lebailly, P. Dynamics of Farming Systems under the Context of Coastal Zone Development: The Case of Xuan Thuy National Park, Vietnam. *Agriculture* **2019**, *9*, 138. [CrossRef]

42. Rouse, J.W.J.; Haas, R.H.; Schell, J.A.; Deering, D.W. *Monitoring Vegetation Systems in the Great Plains with Erts*; NASA Special Publication: Greenbelt, MD, USA, 1974; Volume 351, p. 309.

43. Tucker, C. Red and photographic infrared linear combinations for monitoring vegetation. *Remote Sens. Environ.* **1979**, *8*, 127–150. [CrossRef]

44. Delegido, J.; Verrelst, J.; Alonso, L.; Moreno, J.F. Evaluation of Sentinel-2 Red-Edge Bands for Empirical Estimation of Green LAI and Chlorophyll Content. *Sensors* **2011**, *11*, 7063–7081. [CrossRef]

45. Blackburn, G.A. Quantifying Chlorophylls and Caroteniods at Leaf and Canopy Scales: An Evaluation of Some Hyperspectral Approaches. *Remote Sens. Environ.* **1998**, *66*, 273–285. [CrossRef]

46. Huete, A. A soil-adjusted vegetation index (SAVI). *Remote Sens. Environ.* **1988**, *25*, 295–309. [CrossRef]

47. Frampton, W.J.; Dash, J.; Watmough, G.; Milton, E.J. Evaluating the capabilities of Sentinel-2 for quantitative estimation of biophysical variables in vegetation. *ISPRS J. Photogramm. Remote Sens.* **2013**, *82*, 83–92. [CrossRef]

48. Daughtry, C.; Walthall, C.; Kim, M.; de Colstoun, E.; McMurtrey, J. Estimating Corn Leaf Chlorophyll Concentration from Leaf and Canopy Reflectance. *Remote Sens. Environ.* **2000**, *74*, 229–239. [CrossRef]

49. Freeman, A.; Durden, S.L. A three-component scattering model for polarimetric SAR data. *IEEE Trans. Geosci. Remote Sens.* **1998**, *36*, 963–973. [CrossRef]

50. Krogager, E.; Boerner, W.M.; Madsen, S. Feature-motivated Sinclair matrix (sphere/diplane/helix) decomposition and its application to target sorting for land feature classification. In Proceedings of the SPIE Conference on Wideband Interferometric Sensing and Imaging Polarimetry, San Diego, CA, USA, 1 January 1997.

51. Bayes Classifier. In *Encyclopedia of Database Systems*; Liu, L., Özsu, M.T., Eds.; Springer: New York, NY, USA, 2009; p. 210.

52. Lin, H.T.; Lin, C.J.; Weng, R.C. A note on Platt's probabilistic outputs for support vector machines. *Mach. Learn.* **2007**, *68*, 267–276. [CrossRef]

53. Xue, D.; Hong, Z.; Guo, S.; Gao, L.; Wu, L.; Zheng, J.; Zhao, N. Personality Recognition on Social Media With Label Distribution Learning. *IEEE Access* **2017**, *5*, 13478–13488. [CrossRef]

54. Miller, D.J.; Zhang, Y.; Kesidis, G. Decision Aggregation in Distributed Classification by a Transductive Extension of Maximum Entropy/Improved Iterative Scaling. *EURASIP J. Adv. Signal Process.* **2008**, *2008*, 674974. [CrossRef]

55. Bazaraa, M.S.; Shetty, C.M. *Nonlinear Programming: Theory and Algorithms*; Wiley: New York, NY, USA, 1979.

56. Kearns, M.; Ron, D. Algorithmic stability and sanity-check bounds for leave-one-out cross-validation. *Neural Comput.* **1999**, *11*, 1427–1453. [CrossRef]

57. Zhen, J.; Liao, J.; Shen, G. Mapping Mangrove Forests of Dongzhaigang Nature Reserve in China Using Landsat 8 and Radarsat-2 Polarimetric SAR Data. *Sensors* **2018**, *18*, 4012. [CrossRef]

58. Ferrentino, E.; Nunziata, F.; Zhang, H.; Migliaccio, M. On the Ability of PolSAR Measurements to Discriminate Among Mangrove Species. *IEEE J. Sel. Top. Appl. Earth Obs. Remote Sens.* **2020**, *13*, 2729–2737. [CrossRef]

59. Silva, J.; Bacao, F.; Caetano, M. Specific Land Cover Class Mapping by Semi-Supervised Weighted Support Vector Machines. *Remote Sens.* **2017**, *9*, 181. [CrossRef]

60. Weinstein, B.G.; Marconi, S.; Bohlman, S.; Zare, A.; White, E. Individual Tree-Crown Detection in RGB Imagery Using Semi-Supervised Deep Learning Neural Networks. *Remote Sens.* **2019**, *11*, 1309. [CrossRef]

61. Malouf, R. A Comparison of Algorithms for Maximum Entropy Parameter Estimation. In Proceedings of the Sixth Conference on Natural Language Learning (CoNLL-2002), Taipei, Taiwan, 21 August–1 September 2002; Roth, D., van den Bosch, A., Eds.; ACL: Stroudsburg, PA, USA, 2002.

62. Nocedal, J.; Wright, S.J. *Numerical Optimization*, 2nd ed.; Springer: New York, NY, USA, 2006.

Publisher's Note: MDPI stays neutral with regard to jurisdictional claims in published maps and institutional affiliations.